

Comparison of Approaches for Predicting Solute Transport: Sandbox Experiments

by Walter A. Illman¹, Steven J. Berg², and Tian-Chyi Jim Yeh³

Abstract

The main purpose of this paper was to compare three approaches for predicting solute transport. The approaches include: (1) an effective parameter/macrodispersivity approach (Gelhar and Axness 1983); (2) a heterogeneous approach using ordinary kriging based on core samples; and (3) a heterogeneous approach based on hydraulic tomography. We conducted our comparison in a heterogeneous sandbox aquifer. The aquifer was first characterized by taking 48 core samples to obtain local-scale hydraulic conductivity (K). The spatial statistics of these K values were then used to calculate the effective parameters. These K values and their statistics were also used for kriging to obtain a heterogeneous K field. In parallel, we performed a hydraulic tomography survey using hydraulic tests conducted in a dipole fashion with the drawdown data analyzed using the sequential successive linear estimator code (Yeh and Liu 2000) to obtain a K distribution (or K tomogram). The effective parameters and the heterogeneous K fields from kriging and hydraulic tomography were used in forward simulations of a dipole conservative tracer test. The simulated and observed breakthrough curves and their temporal moments were compared. Results show an improvement in predictions of drawdown behavior and tracer transport when the K tomogram from hydraulic tomography was used. This suggests that the high-resolution prediction of solute transport is possible without collecting a large number of small-scale samples to estimate flow and transport properties that are costly to obtain at the field scale.

Introduction

Improving our ability to predict the temporal and spatial evolution of solute transport at high resolution in geologic media has been a topic of great interest over the past few decades. The recognition of the importance of the spatial variability of hydraulic conductivity (K) for understanding and predicting solute transport in geologic media, as well as the quantification of associated uncertainty has

led to the development of various stochastic effective parameter/macrodispersivity approaches (Gelhar 1993). These approaches use the spatial statistics of small-scale K to derive the upscaled effective K for an equivalent homogeneous medium of the true heterogeneous medium; then, macrodispersivity is applied to account for the effects of spatial variability of small-scale K on solute transport that were omitted in the estimation of the effective K . The stochastic effective parameter approaches have yielded much optimism about our abilities to predict solute transport behavior both spatially and temporally over the past few decades. For example, various field (MacKay et al. 1986; LeBlanc et al. 1991; Boggs et al. 1992) and laboratory experiments (Fernández-García et al. 2005 and others) have been conducted to show the applicability of the effective K and macrodispersivity approach (Sudicky 1986; Sudicky et al. 2010).

Limitations of these effective hydraulic parameter/macrodispersivity approaches for predicting fine-scale behavior of the tracer plume were demonstrated through tracer experiments at the MADE (Rehfeldt et al. 1992)

¹Corresponding author: Waterloo Institute for Groundwater Research, Department of Earth & Environmental Sciences, University of Waterloo, Waterloo, Ontario N2L 3G1, Canada; willman@uwaterloo.ca

²Waterloo Institute for Groundwater Research, Department of Earth & Environmental Sciences, University of Waterloo, Waterloo, Ontario N2L 3G1, Canada.

³Department of Hydrology and Water Resources, University of Arizona, Tucson, AZ.

Received February 2011, accepted July 2011.

© 2011, The Author(s)

Ground Water © 2011, National Ground Water Association.

doi: 10.1111/j.1745-6584.2011.00859.x

and Georgetown (Yeh et al. 1995b) sites. In particular, Mas-Plas et al. (1992) and McCarthy et al. (1996) conducted two-well, forced-gradient tracer experiments in a coastal sandy aquifer. The results of this tracer test were modeled using a three-dimensional (3D) flow and transport model (Yeh et al. 1995b). The results revealed that using the effective K and macrodispersivity can satisfactorily produce the bulk behavior of the chloride breakthrough observed at the pumping well, but the preferential migration of tracer can only be captured using the detailed 3D K field obtained from a large number of slug tests. These results corroborate the view of Yeh (1992) that the upscaled effective K and macrodispersivity approaches are practical and useful. However, they can yield only the bulk behavior of solute migration in the subsurface, and thus serve, at best, as a tool for a first-cut analysis. In order to meet the resolution of interest, more detailed information on the spatial distribution of small-scale K heterogeneity is needed.

Recently, hydraulic tomography has been developed (Gottlieb and Dietrich 1995; Yeh and Liu 2000; Bohling et al. 2002; Brauchler et al. 2003; Zhu and Yeh 2005, 2006; Li et al. 2005; Fienen et al. 2008; Castagna and Bellin 2009; Xiang et al. 2009; Liu and Kitanidis 2011) to obtain higher resolution K estimates. Because it is a new technology, laboratory experiments have been conducted (Liu et al. 2002; Illman et al. 2007, 2008; 2010a, 2010b; Liu et al. 2007; Yin and Illman 2009; Berg and Illman 2011, Berg and Illman (unpublished data)) to evaluate hydraulic tomography, while several field experiments (Bohling et al. 2007; Li et al. 2007; Straface et al. 2007; Illman et al. 2009; Cardiff et al. 2009; Berg and Illman (unpublished data)) have also been reported that show that the technique can image K heterogeneity. Recently, Ni et al. (2009) conducted numerical simulations to show that hydraulic tomography is able to capture a sufficient spatial distribution of K so that detailed, high-resolution, solute transport behaviors in aquifers can be predicted. However, these promising results have not been demonstrated to date either in the laboratory or in the field.

The main objective of this paper is to compare two widely accepted approaches and one new approach for predicting solute transport in a controlled sandbox experiment. The two widely accepted methods are: (1) the effective parameter approach of Gelhar and Axness (1983); (2) the heterogeneous approach based on point samples of K and ordinary kriging; and the new approach is (3) the heterogeneous approach based on a K distribution (or K tomogram from now on) obtained from hydraulic tomography.

Experimental Methods

Sandbox Aquifer Construction

A synthetic heterogeneous aquifer was constructed in a vertical, laboratory sandbox to evaluate the three approaches. The sandbox is 193.0 cm in length, 82.6 cm in height, and has a depth of 10.2 cm. A layered

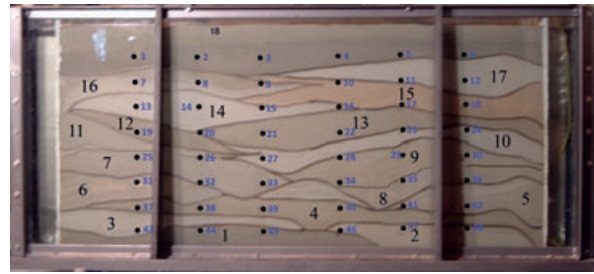


Figure 1. Photograph of the sandbox showing the synthetic heterogeneous aquifer in which the dipole cross-hole and conservative tracer tests were conducted. Large black numbers indicate layer numbers, solid circles indicate port locations, and small blue numbers indicate port numbers. Layer 1 = 20/30; layer 2 = 40/30; layer 3 = F85; layer 4 = 20/40; layer 5 = mix; layer 6 = mix; layer 7 = #12; layer 8 = F32; layer 9 = 20/40; layer 10 = F65; layer 11 = #12; layer 12 = 16/30; layer 13 = 20/30; layer 14 = F75; layer 15 = 20/40; layer 16 = mix; layer 17 = F85; layer 18 = 20/30. Note: The layers labeled “mix” consisted of equal volumes of #14, F75, and 16/30 sands (modified from Illman et al. 2010a).

deposit was created through the cyclic flux of sediment-laden water under varying water flow and feed rates of sediments (Illman et al. 2010a).

To instrument the aquifer, 48 ports, 1.3 cm in diameter, have been cut out of the stainless steel wall of the flow cell to allow coring of the aquifer as well as installation of horizontal wells. The wells, which penetrate the horizontal thickness of the synthetic aquifer, were installed after the deposition of the layers. Each well location is monitored by a pressure transducer, and can be used for pumping, injection of tracers, or for sampling. Figure 1 is a photograph of the frontal view of the synthetic aquifer, showing the interfingering nature of the deposits with numbers indicating the layers. Port locations are also shown on this figure. Further details to this synthetic heterogeneous aquifer and its construction approach are provided in Illman et al. (2010a).

Pressure measurements were made with 50 Setra model 209 gauge pressure transducers with a range of 0 to 1 psi, 48 of which measured hydraulic head in the aquifer. These pressure transducers were installed at each of the 48 ports in the stainless steel wall of the sandbox.

For this particular study, all boundaries around the synthetic aquifer were set as no-flow boundaries to achieve better mass control for the hydraulic and tracer experiments. This was found to be critical during our initial studies as our previous sandboxes had constant head reservoirs which could potentially diminish the tracer signals via dilution.

Aquifer Characterization Methods

Permeameter Analysis of Core Samples

We first determined the K of the sands from the 48 horizontal cores obtained during the installation of 48 wells. These cores were then attached to a custom-made constant head permeameter for determination of

K . Details of the core extraction method and the design of the constant head permeameter is provided in Craig (2005). The K values from cores are calculated using Darcy's law.

Dipole Hydraulic Tomography Tests

Hydraulic tomography tests were conducted by pumping water from one well and injecting the pumped water at another location (dipole hydraulic tomography tests from now on) and then monitoring changes in hydraulic heads at other ports in the sandbox. In these tests, a mass balance of water injected and extracted was maintained using a peristaltic pump by connecting the injection and extraction ports in a single loop. Eight pairs of ports consisting of tests 1 through 8 (e.g., test 1: extraction at port 2 and injection at port 47, from now on E2/I47 [E=Extraction port and I for injection port]; test 2: E42/I7; test 3: E4/I45; test 4: E15/I34; test 5: E24/I25; test 6: E17/I32; test 7: E23/I26; and test 8: E20/I29) were chosen for these tests (see Figure 1 for port locations). Injection and pumping rates for all tests averaged 480 mL/min. Prior to each test, all pressure transducers were calibrated to ensure accurate data collection. We then collected hydraulic head data for several minutes in all pressure transducers to establish a static, initial condition. After establishment of static conditions, we pumped from each port using a peristaltic pump, injecting the pumped water into another port, while taking head measurements at all 48 ports. For each test, pumping continued until the development of steady-state conditions, which was determined by observing the stabilization of all head measurements. After each dipole test, the pumps were shut down for a period of time to allow the water in the sandbox to return to the initial condition. This was repeated for each test.

Dipole Conservative Tracer Test

Description of Dipole Conservative Tracer Test

After the dipole hydraulic tomography tests, we conducted a dipole tracer test using bromide as a conservative tracer. Prior to the injection of the tracer, a dipole flow field was established by injecting tap water at port 42 at a rate of 372.4 mL/min and extracting at port 7 at 304 mL/min. A water mass balance was then achieved by setting 12 sampling lines at a cumulative rate of 68.4 mL/min. Figure 2 is a schematic diagram showing the injection, extraction, and sampling ports for the test.

Once steady-state flow conditions were reached (injection, extraction, and sampling rates were stable and in equilibrium) a valve in the injection line was switched from water to a solution containing bromide (Fisher Scientific, Pittsburgh, Pennsylvania) as the conservative tracer (151.3 mg/L). Food coloring (70 mL of blue "Tone's" Food Coloring) was added to the tracer solution so that we could observe the movement of the tracer plume in the sandbox through the glass. The tracer solution was injected for 10 min and then the injection line was switched back to tap water. Each of the sampling ports

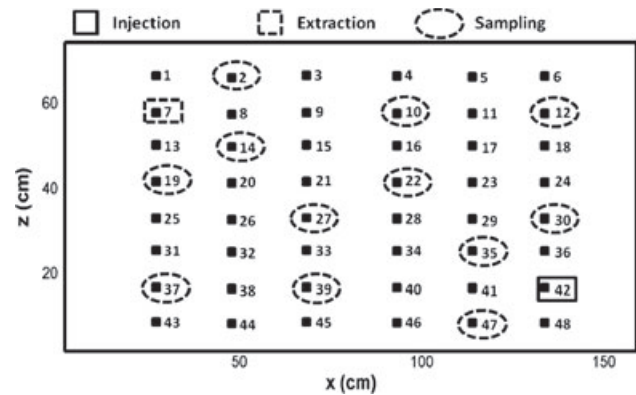


Figure 2. Schematic diagram showing the injection, extraction, and sampling ports during the dipole conservative tracer test.

(and the main extraction port) were sampled over a period of 5 h to record the movement of the bromide tracer through the aquifer. Sixty water samples were collected from each of the 12 sampling lines (plus the effluent line) during the dipole tracer test for a total of 780 samples. Upon completion of the experiment, conservative tracer (Br^-) concentrations were determined using an ion chromatograph (IC) (Dionex ICS 2000, Dionex, Sunnyvale, California) equipped with an AS40 auto sampler.

Heterogeneity Characterization Methods

Geostatistical Analysis and Kriging of Core K Estimates

Geostatistical analysis of the 48 core K data was conducted using the Surfer 8 (www.goldensoftware.com). The exponential variogram model was used to fit the experimental variograms in both horizontal and vertical directions, resulting in an anisotropic variogram model. The variogram parameters for the experimental variograms to be used in kriging thus included the geometric mean ($K_G = 0.08$ cm/s), the variance ($\sigma_{\ln K}^2 = 0.87$) and the correlation lengths ($\lambda_x = 60$ cm and $\lambda_z = 20$ cm).

We then kriged the core K estimates using this anisotropic variogram model. The kriged domain was discretized into 73 vertical elements and 162 horizontal elements. Figure 3 shows the kriged K field which delineates some of the major layers, but definitely has



Figure 3. K distribution obtained through kriging of core scale K data from permeameter analysis.

a smoothed appearance. Effects of correlation lengths on the estimate were investigated and were found to be insignificant due to density of the samples and the small size of the sandbox.

Estimates of Effective Hydraulic Conductivity and Macrodispersivity

The stochastic theory of Gelhar and Axness (1983) provides a methodology for determining large-scale effective flow and transport parameters (i.e., effective K and macrodispersivity) from the knowledge of spatial statistics (mean, variance, and correlation scales) describing the spatial variations of the underlying local-scale $\text{Ln}(K)$ process (from now on, $Y = \text{Ln}(K)$). This theory assumes that if the local-scale mixing process is sufficient, the flow and transport processes will reach the ergodic condition, where the ensemble mean flow and transport behaviors derived from the stochastic approaches will be equivalent to those observed in the field.

The relationship between the asymptotic macrodispersivity tensor (A_{ii} , $i = 1$ and 2) where 1 and 2 denotes x and z direction, respectively, and the spatial statistics describing the spatial variability of the K field have been derived by Gelhar and Axness (1983) under the assumption of uniform flow. For the case of statistical anisotropy in the vertical and horizontal directions where $\lambda_1 > \lambda_2 > \lambda_3$ (case 2, Gelhar and Axness 1983), the longitudinal macrodispersivity A_{11} is given by

$$A_{11} = \sigma_Y^2 \lambda_1 \lambda_2 / [\xi^2 (\lambda_1^2 \sin^2 \phi + \lambda_2^2 \cos^2 \phi)^{1/2}] \quad (1)$$

where

$$\xi = \exp[\sigma_Y^2 (0.5 - g_{22})] / (\sin^2 \phi + \bar{K}_{22} / \bar{K}_{11} \cos^2 \phi) \quad (2)$$

and

$$A_{11} = \sigma_Y^2 \lambda_1. \quad (3)$$

Here, the flow integrals, g_{ii} ($i = 1, 2$) are functions of the correlation lengths defined by Gelhar and Axness (1983), σ_Y^2 is the variance of Y , and ϕ is the angle in the horizontal plane between the mean flow direction and the longitudinal axis of the effective K tensor (\bar{K}_{ii}). It should be noted that a longitudinal macrodispersion coefficient calculated using (3) must be augmented by the value of the local longitudinal dispersion coefficient. When the mean flow direction coincides with the λ_1 direction ($\phi = 0^\circ$), the transverse macrodispersivity values are zero, thus indicating that the transverse macrodispersion process is controlled by local transverse dispersion. The effective K tensor used earlier is given by

$$\bar{K}_{ii} = K_g \exp[\sigma_Y^2 (0.5 - g_{ii})]. \quad (4)$$

Using estimated values for λ_1 and λ_2 equal to 60 and 20 cm, respectively, and a variance of $\sigma_Y^2 = 0.87$, as estimated from the two-dimensional (2D) variogram analysis, the principal values of the effective K tensor are

given as $K_{11} = 0.096$ cm/s and $K_{22} = 0.062$ cm/s for the permeameter estimates of K . The computed value of the longitudinal macrodispersivity using Equation (3) equals 52.08 cm on the basis of the geostatistical parameters derived from the 2D variogram analysis.

Analysis of Dipole Hydraulic Tomography Tests

Inverse Modeling Approach

The steady-state analysis of dipole hydraulic tomography tests was conducted using a sequential successive linear estimator (SSLE) approach (Yeh and Liu 2000). To obtain a K tomogram from the available tests, we solved an inverse problem for steady-state flow conditions. Boundary conditions were set to be no-flow for all sides. We created a fine grid with the synthetic aquifer discretized into 11,826 elements and 24,124 nodes with element dimensions of 1.0 cm \times 10.2 cm \times 1.0 cm.

Inputs to the inverse model include the mean, variance and the correlation scales for K , volumetric discharge (Q_n) from each pumping test where n is the test number, as well as steady-state head data. The mean, variance, and the correlation scales used here are identical to those in the kriging analysis.

For the analysis, we used the eight dipole hydraulic tomography tests (test 1: E2/I47; test 2: E42/I7; test 3: E4/I45; test 4: E15/I34; test 5: E24/I25; test 6: E17/I32; test 7: E23/I26; and test 8: E20/I29) and the corresponding steady-state head observations at the rest of 46 ports during each test as data sets. The steady-state head value from each port was obtained by averaging the steady-state portion of the record. We elected to not use the head data from the injection and extraction ports from each test because these ports could be affected by skin effects (Illman et al. 2007). Further details on preprocessing of hydraulic head data can be found in Illman et al. (2007, 2008) and Xiang et al. (2009).

Figure 4 is the K tomogram obtained by inverting the steady-state head data from eight tests. Spatial statistics of this estimated K tomogram are the geometric mean ($K_G = 0.15$ cm/s), the variance ($\sigma_Y^2 = 1.70$), and the correlation lengths ($\lambda_x = 60$ cm and $\lambda_z = 20$ cm).

It is of interest to note that the variance estimated from SSHT ($\sigma_Y^2 = 1.70$) is higher than the estimated value $\sigma_Y^2 = 0.87$ from the geostatistical analysis of core samples. These values are in turn higher than those determined at the Cape Cod site ($\sigma_Y^2 = 0.14$) (Wolf 1988), and the CFB Borden site ($\sigma_Y^2 = 0.29$) (Sudicky 1986), but is significantly lower than the MADE site ($\sigma_Y^2 = 4.50$) (Rehfeldt et al. 1992) or the North Campus Research Site on the University of Waterloo campus ($\sigma_Y^2 = 6.50$) (Alexander et al. 2010).

Results: Dipole Tracer Test

Six photo snapshots of tracer plume evolution throughout the experiment were taken at $t = 12, 27, 62, 100, 175,$ and 286 min (Figure 5a to 5f). At $t = 0$ min, the injection of the tracer solution began and at $t =$

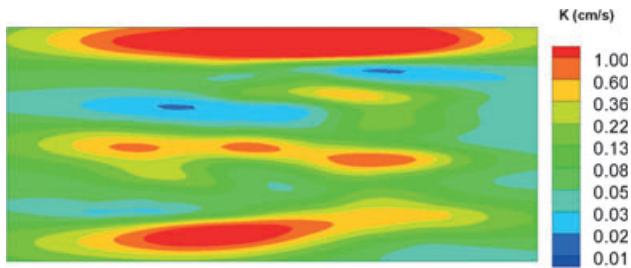


Figure 4. K tomogram computed using the steady-state hydraulic tomography algorithm of Yeh and Liu (2000).

10 min, the injection was switched from tracer solution to tap water. The snapshots were utilized for qualitative assessment of the tracer migration.

Figure 5a was taken at $t = 12$ min, 2 min after the injection of the tracer solution at port 42 completed in layer 5 ended. Layer 5 consisted of a mixture of #14, F75, and 16/30 sands. We notice from this figure that the tracer solution uniformly distributes in layer 5. However, this figure also shows that the tracer solution is preferentially transported along layer 4 (20/40) which has a K of 2.05×10^{-1} cm/s.

At 27 min (Figure 5b), 17 min after the injection was switched from tracer solution to tap water, we notice that the blue dye becomes cleared around the injection port. Figure 5b shows that the tracer continues to move rapidly through layer 4. The tracer solution also moves laterally and upwards through layer 8 (F32), layer 9 (20/40), and into layer 10 (F65).

At 62 min (Figure 5c), we notice that the tracer solution becomes more diluted through the injection of tap water. We also notice that the tracer has migrated into layers 13 (20/30) and 15 (20/40). It also begins to migrate into layer 17 (F85) which has the lowest K in the aquifer at 1.35×10^{-2} cm/s.

At 100 min (Figure 5d), the tracer appears to breakthrough layer 17 (F85) vertically and reaches layer 18 (20/30). Because of the high K of the 20/30 sand

(3.12×10^{-1} cm/s), the tracer then rapidly migrates laterally through layer 18. The tracer also appears to migrate rapidly through layer 7 (#12) which has a K of 2.05×10^{-1} cm/s.

By 175 min (Figure 5e), the tracer appears to reach port 7 which is the extraction port that is completed in layer 14 (F75). We notice that despite the fact the tracer solution appears to be diluted, the tracer plume has reached most parts of the aquifer and all of the layers between the injection and extraction ports.

By 286 min (Figure 5f), we observe that the tracer has been removed from the high K layers. However, there is a noticeable amount of blue dye in low K layers including: layer 3, layer 8, layer 10, layer 14, and layer 17. This suggests that the low K layers can contribute to store tracers for a long period requiring a long period to flush the tracers out of the synthetic aquifer. Breakthroughs of the tracer during the experiment are shown in Figure 8.

Prediction of Dipole Tracer Test

Description of Tracer Transport Simulations

A 2D, saturated flow and transport model of the synthetic aquifer was developed using the finite-element code VSAFT2 (Yeh et al. 1993). For the effective parameter approach, we utilized the effective hydraulic conductivity (K_{eff}) to simulate groundwater flow during the dipole tracer test, and a longitudinal macrodispersivity (A_{11}) to simulate the migration of the conservative tracer. To address the issue that dipole tracer tests conducted in a bounded aquifer could potentially yield smaller dispersivity estimates, we also conducted an additional simulation with macrodispersivity reduced by 30% to examine its sensitivity to tracer transport. We also simulated groundwater flow and plume migration using the kriged K field and the K tomogram. For the transport simulation using the kriged K field and the K tomogram, we set the dispersivity value equal to zero, while the effective porosity was set to 0.36 for all cases. In total, three different cases were considered.

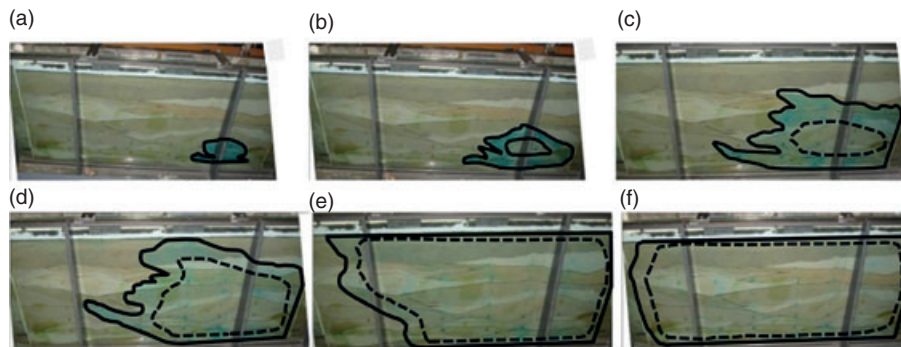


Figure 5. Photographs of sandbox during the tracer test at various times: (a) $t = 12$ min; (b) $t = 27$ min; (c) $t = 62$ min; (d) $t = 100$ min; (e) $t = 175$ min; and (f) $t = 286$ min. The solid line represents the edges of the dyed tracer plume. The dashed lines are approximations of the extent of the tracer plume. Note: at $t = 175$ and $t = 286$, most of the dye has left the system, however, some dye is trapped around the wells ever after the tracer has been flush through the system giving the tank a blue-green tinge at these times.

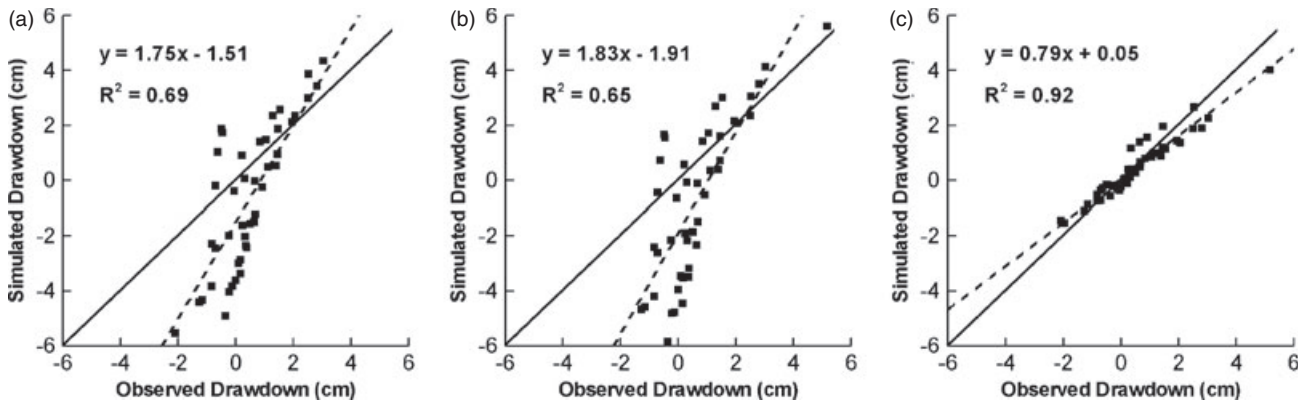


Figure 6. Simulated vs. observed drawdowns at 48 ports during the dipole tracer test. Simulated values were computed using: (a) K_{eff} from Gelhar and Axness (1983) solution with statistics of permeameter analysis of core samples; (b) kriged K field; and (c) K tomogram.

For all cases, flow conditions were established by simulating steady-state flow with injection, extraction, and sampling ports. A tracer solution with a bromide concentration of 151.3 mg/L is then injected for 10 min and solute transport is simulated under transient conditions. As in the experiment, all boundaries are set as no-flow and no-flux boundaries.

Groundwater Flow Results

Figure 6a shows scatter plots of simulated vs. observed steady-state drawdown values during the dipole tracer test at the sampling ports using the K_{eff} based on the Gelhar and Axness (1983) formula. Likewise, Figure 6b shows the same when the kriged K field is used while Figure 6c illustrates the predicted vs. observed drawdowns using the K tomogram. These comparisons show that the K_{eff} and kriged K field both yield biased predictions of drawdowns at various locations in comparison to that based on the K tomogram. In addition, predicted drawdown based on the K_{eff} and that based on kriged K field exhibit greater bias and scattering. In contrast, the K tomogram yields improved results.

Dipole Tracer Test Simulation Results

Figure 7a shows the spatial distribution of tracer concentrations at various times using the K_{eff} and macrodispersivity estimates. The results reveal that the concentration distribution evolves quite uniformly with significant spreading of the tracer concentration. Not shown here are results of simulations in which we reduced the macrodispersivity by 30%. As expected, reducing macrodispersivity by 30% did not significantly influence our results due to the dipole flow field.

Figure 7b is the result using the kriged K field while Figure 7c is the result based on the K tomogram. We note that dispersivity was set to zero for both cases. Both Figure 7b and 7c show that due to the mapping of the heterogeneity, the concentration distributions are less smooth in comparison to the effective parameter case (Figure 7a). These figures reveal a much more heterogeneous distribution of tracer concentrations with

tracers following preferential pathways with hydraulic tomography providing a more heterogeneous concentration distribution in comparison to kriging.

We next compare the results from Figure 7a through 7c with the tracer snapshots in Figure 5a through 5c. The time of the snapshot and that of the transport simulation results are not exactly coincident, but the two figures nonetheless can be compared qualitatively. The comparison shows that the migration of the tracer represented by the migration of the dye is better represented by Figure 7b and best represented by Figure 7c. This is expected as the transport simulations involving effective parameters do not consider the K heterogeneity, while kriging and hydraulic tomography yields increasingly realistic distributions of K heterogeneity that can better represent the migration of tracers.

While results are not presented here, we also examined the impact of porosity (ϕ) heterogeneity on the tracer transport. Using grain size information and the estimated K values, a heterogeneous ϕ field was created. Using both the heterogeneous K from hydraulic tomography and ϕ together showed a marginal improvement in tracer simulation. However, as K varied over a much greater range than ϕ , it was found to be significantly more important in determining the migration of the tracer.

Simulated vs. Observed Breakthrough Curves

We next make a direct comparison of the breakthrough curves obtained through numerical simulations and the actual tracer data (Figure 8a to 8c). The matches of the breakthrough curves (Figure 8a) obtained from ports (30, 35, and 47) close to the injection port are quite good for all cases. In particular, the arrival time, peak concentrations, and time for tracer concentrations to reach background levels is quite consistent for all cases.

Differences in the quality of matches begin to emerge when the breakthrough curves from the intermediate distance ports (10, 12, 22, 27, 37, and 39) are examined (Figure 8b). We observe that case 1 (effective parameters) consistently underpredicts the peak concentration at all

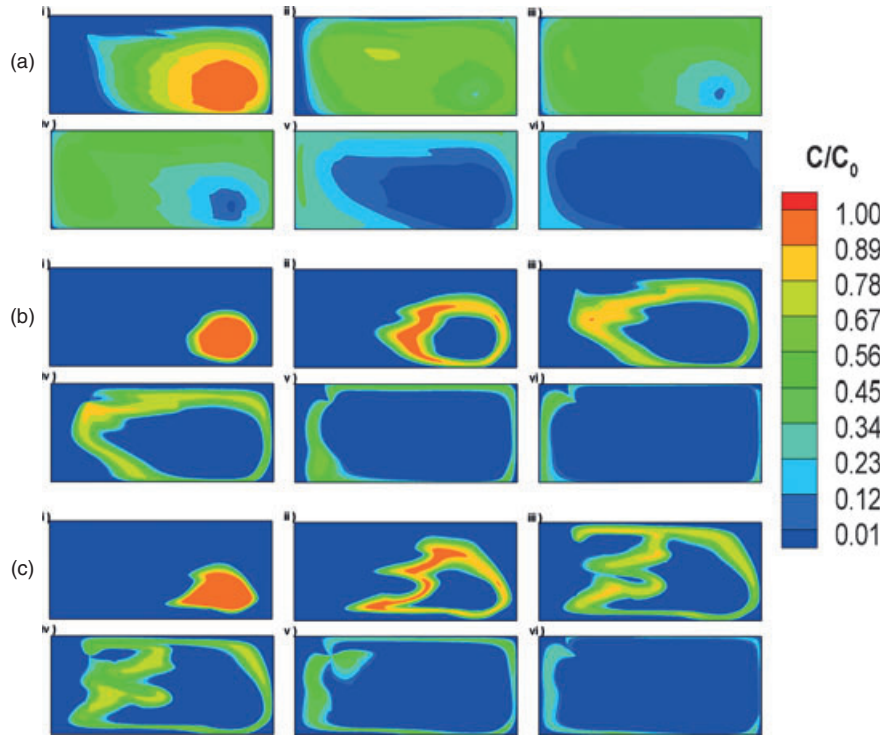


Figure 7. Concentration distributions from tracer transport simulation with: (a) K_{eff} and A_{11} computed using Gelhar and Axness (1983) solution with statistics of K from the permeameter analysis of core samples (case 1); (b) kriged K field (case 2); and (c) K tomogram (case 3). Snapshots of concentration distributions are from (i) $t = 10$ min, (ii) $t = 30$ min, (iii) $t = 60$ min, (iv) $t = 100$ min, (v) $t = 170$ min, and (vi) $t = 290$ min for all cases.

ports in this category and show an earlier arrival of tracers. In contrast, cases 2 (kriging) and 3 (K tomogram) show a marked improvement in the quality of the fits with case 3 performing the best visually, on the average.

Examination of the furthest ports (2, 14, 19) from the injection port (Figure 8c) shows mixed results. In general, we observe that case 3 performs better than cases 1 and 2 in terms of better predicting the peak concentrations and arrival times of tracers. However, we also note that the matches are far from perfect.

At the extraction port (7), none of the three approaches yields a perfect prediction (Figure 8c), however, we find case 3 captures the first 2 peaks that arrive at different times. Case 1, on the other hand, because it is based on the effective parameter approach, cannot capture the multiple peak behavior. Likewise, case 2 with the smoother K field does not capture this behavior. To compare results quantitatively, we next compute and compare the temporal moments.

Temporal Moment Analysis

The temporal moment analysis was used to characterize the breakthrough data at all wells. The n th temporal moments (M_n) of concentration (C) at location (x, y) at time (t) are given by:

$$M_n = \int_0^{\infty} t^n C(x, y, t) dt \quad (5)$$

where t is time, $C(x_i, t)$ is tracer concentration. One can compute the zeroth (M_0), first (M_1), and second (M_2) temporal moments using the moment generating function (Equation 5) by setting $n = 0, 1$, and 2 , respectively. The temporal moments were obtained through numerical integration of the breakthrough data using the trapezoidal rule.

The total mass of solute passing through the sandbox at each sampling point is obtained by computing the M_0 from the breakthrough curves. The first normalized moment of breakthrough curves at each sampling ports were used to estimate the mean arrival time of the center of bromide mass (μ):

$$\mu = \frac{M_1}{M_0} \quad (6)$$

The variance (σ^2) of the breakthrough curve is then calculated by

$$\sigma^2 = \frac{M_2}{M_0} - \left(\frac{M_1}{M_0} \right)^2 \quad (7)$$

In general, the σ^2 represents the spread of the concentration distribution and is influenced by mechanical dispersion and molecular diffusion.

Figure 9a to 9c shows the M_0 , μ , and σ^2 computed from the temporal moment analyses of simulated and observed breakthrough curves. In particular, Figure 9a reveals the estimates of M_0 at these observation ports are, on average, higher for the simulated breakthrough curves

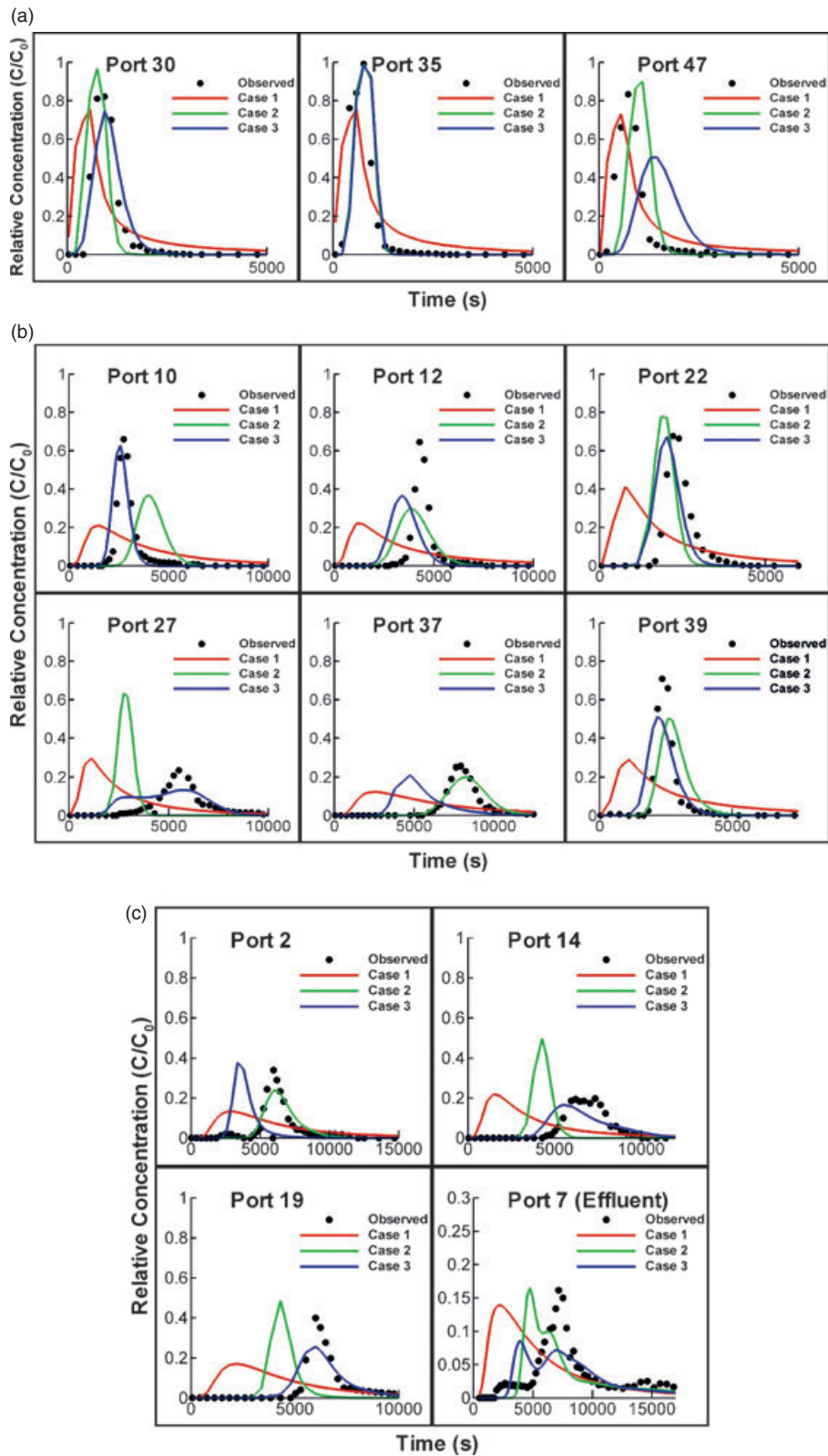


Figure 8. Breakthrough curves from the dipole tracer test and corresponding match of forward simulations (a) near the injection port, (b) at intermediate distances, and (c) at large distances from the injection port.

for case 1. Figure 9a also indicates that when the heterogeneity in K is considered (i.e., cases 2 and 3), the estimation of the total mass at a given sampling point improves. This suggests that the heterogeneity estimated

by kriging and hydraulic tomography appears to capture the flow paths of the tracer reaching these sampling ports.

The arrival time of the center of mass (μ) for the three cases is plotted in Figure 9b. Results of the three cases

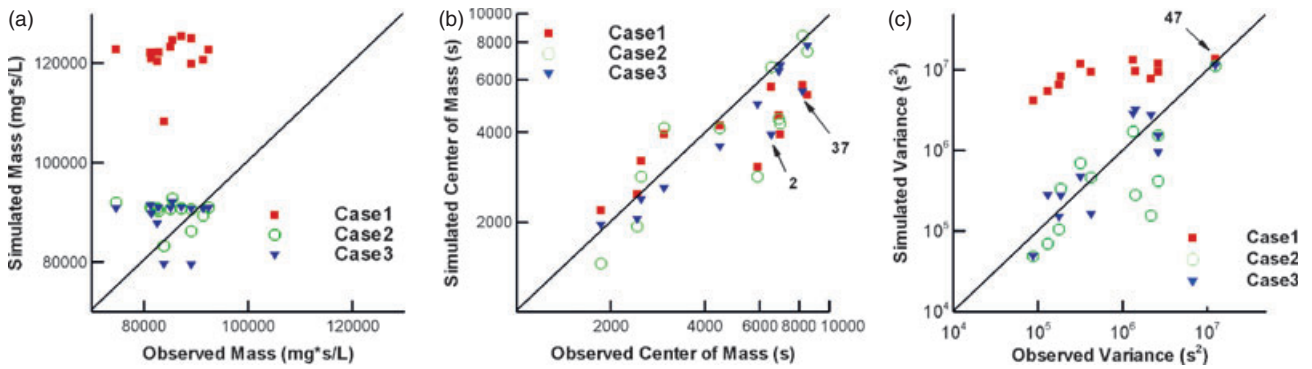


Figure 9. (a) Total mass (M_0), (b) mean arrival time (μ), and (c) variance (σ^2) of the breakthrough curves at each sampling port for cases 1–3.

show that the arrival times of simulated breakthroughs for the ports close to the injection port are similar to those observed. At ports that are far away from the injection point, the discrepancy between the simulated and observed values increases. While the scatter is centered around the 1:1 line for all cases, case 3 shows less scatter. There are two sampling points 2 and 37 that causes the simulated vs. observed relationship to be biased at larger times. These two ports are at a large travel distance and near boundaries where there are no observation points hence making the estimated K tomogram in these areas more uncertain. If we choose to disregard these two points, then the relationship between the simulated and observed values becomes stronger. This suggests that the mapping of heterogeneity via hydraulic tomography yields more accurate estimates of the arrival times of the center of mass for this synthetic aquifer.

The σ^2 of the breakthrough curves was also calculated at each sampling point and plotted on Figure 9c. The result suggests that the approach based on effective parameters over predicts the temporal spreading of the plume which is also evident in Figure 7a. The σ^2 estimates at the extraction point (port 47) for case 1 are, however, satisfactory, suggesting that an integrative behavior (such as breakthrough at the extraction well) can be predicted by low-spatial resolution approach. When we examine case 2 in which the kriged K field is used, the bias in the σ^2 estimates diminishes at sampling intervals close to the injection well. In contrast, a remarkable improvement is seen in case 3 in which both the bias and scatter diminish considerably. This suggests that hydraulic tomography can adequately map the heterogeneity, which leads to a higher resolution prediction of the tracer migration. These results are consistent with those obtained by Yeh et al. (1995b) at Georgetown site, where detailed heterogeneity was characterized using 308 slug tests.

Discussion and Summary

While our finding that better characterization of heterogeneity leads to better prediction of the flow and solute transport is expected, our study substantiates and quantifies this simple fact. Specifically, we

showed that the effective K approach resulted in biased predictions of drawdowns during the dipole tracer test. In conjunction with the estimated macrodispersivity, it predicted a general spatial pattern of the observed tracer migration at low resolutions. More importantly, we demonstrated that the K tomogram estimated from hydraulic tomography yielded an excellent prediction of drawdowns and better tracer distribution patterns during the dipole tracer test than the effective K approach and the approach based on kriging with core samples.

To our knowledge, formulae for effective K and macrodispersivity do not exist for a dipole tracer test. We therefore adopt Gelhar and Axness (1983)'s formulae to approximate the effective parameters which assumes that transport takes place under uniform flow conditions. For a dipole flow condition, macrodispersivity is expected to be smaller due to converging/diverging flow. Analysis of our transport predictions by reducing macrodispersivity by 30% however did not alter our results. This is attributed to the fact that the arrival time, peak concentration, and time are mainly controlled by convective flow during the dipole experiment.

There are numerous approaches available for estimating K spatial distribution. One popular approach is geostatistics (i.e., kriging) using point measurements of K as we did in this study. If other measurements such as head, concentration, or other related properties are available, cokriging and other data fusion techniques (such as hydraulic tomography) can be used to improve the estimate based on K measurements alone. For example, Yeh and Zhang (1996), Li and Yeh (1999), and others investigated usefulness of moisture content, tracer, and head measurements for characterizing vadose zones and aquifers using cokriging.

Over the past decade, hydraulic tomography has proved to be a matured technology, but is not widely accepted and understood. As a matter of fact, hydraulic tomography is built upon data fusion concept, and its algorithm (SSLE) for analysis is an extension of kriging or cokriging. Kriging interpolates and extrapolates measured K values to other locations according to variogram (spatial statistical correlation structure) of K 's. Cokriging utilizes both measured K values and observed state

variables (e.g., head) to estimate K at other locations. During the estimation, not only does cokriging takes advantage of the variogram of K as does in kriging but also uses spatial relationship between K and the head field (i.e., considers flow process). Therefore, cokriging in general yield better results than kriging. On the other hand, SSLE overcomes the linear relationship between head and K assumption employed in cokriging (Yeh et al. 1996). It maximizes the information of the measured head data about the K , which may be called an iterative cokriging-like technique (Yeh et al. 1995a). Hydraulic tomography is superior to all these methods because it creates and collects head data of different pumping tests; these data sets have nonredundant information about the K distribution; hydraulic tomography then employs SSLE to estimate the spatially distributed K field.

Without any surprise, both qualitative and quantitative evaluations of predictions of the tracer experiment revealed that mapping detailed heterogeneity using either kriging/core samples or hydraulic tomography can improve the prediction, but hydraulic tomography yielded a better prediction. Nevertheless, we must emphasize that the K tomogram from hydraulic tomography did not capture all the details of tracer breakthrough. This result agrees with the findings by Yeh et al. (1995b) and Konikow (2011) that the prediction of the tracer breakthrough at individual locations in a field is a difficult task.

In comparison with results of the work by Ni et al. (2009), which evaluated these methods for predicting flow and transport under uniform flow using error-free numerical experiments, we attribute the discrepancy in simulated vs. observed breakthrough curves and temporal moments to several factors. They are: (1) the effects of noise in head measurements used in hydraulic tomography, (2) the diverging and converging flow fields forcing tracers to migrate through areas near the impermeable boundaries of the sandbox, where heterogeneity cannot be mapped satisfactorily using hydraulic tomography due to the lack of monitoring points in these areas, and (3) the less diffusive nature of the tracer which demands a much higher resolution mapping of the K field.

These shortcomings may be overcome by deploying a denser monitoring network for the hydraulic tomography tests or through the joint inversion of hydraulic tomography and tracer test data (Yeh and Zhu 2007, Li and Yeh 1999; Illman et al. 2010b). In addition, conditioning of the K tomogram using accurate point scale K data and geophysical surveys may potentially useful. However, this is beyond the scope of the current manuscript, but is a topic for further research.

Finally, our study suggests that hydraulic tomography can improve our predictions of solute transport without collecting a large number of small-scale samples to estimate effective parameters or ascribing dispersivity estimates that are costly to obtain at the field scale through tracer tests. Our results support the call for a change in the way we collect and analyze data for characterizing aquifers (Yeh and Lee 2007).

Acknowledgments

This research was supported by the Strategic Environmental Research and Development Program (SERDP) as well as by funding from the National Science Foundation (NSF) through grants EAR-0229713, EAR-0229717, IIS-0431069, IIS-0431079, EAR-0450336, EAR-0450388, and EAR-1014594. We thank Andy Craig for his assistance in the tracer experiment. We also thank the Editor-in-Chief (Frank Schwartz) and two anonymous reviewers for their comments that led to an improved manuscript.

References

- Alexander, M., S.J. Berg, and W.A. Illman. 2010. Field study of hydrogeologic characterization methods in a heterogeneous aquifer. *Ground Water* 49, no. 3: 365–383. DOI: 10.1111/j.2010.00729.x.
- Berg, S.J., and W.A. Illman. 2011. Capturing aquifer heterogeneity: Comparison of approaches through controlled sandbox experiments. *Water Resources Research*. In press.
- Boggs, J.M., S.C. Young, L.M. Beard, L.W. Gelhar, K.R. Rehfeldt, and E.E. Adams. 1992. Field study of dispersion in a heterogeneous aquifer: 1. Overview and site description. *Water Resources Research* 28, no. 12: 3281–3291. DOI: 10.1029/92WR01756.
- Bohling, G.C., J.J. Butler Jr., X. Zhan, and M.D. Knoll. 2007. A field assessment of the value of steady shape hydraulic tomography for characterization of aquifer heterogeneities. *Water Resources Research* 43, W05430. DOI: 10.1029/2006WR004932.
- Bohling, G.C., X. Zhan, J.J. Butler, Jr, and L. Zheng. 2002. Steady shape analysis of tomographic pumping tests for characterization of aquifer heterogeneities. *Water Resources Research* 38, no. 12: 1324. DOI: 10.1029/2001WR001176.
- Brauchler, R., R. Liedl, and P. Dietrich. 2003. A travel time based hydraulic tomographic approach. *Water Resources Research* 39, no. 12: 1370. DOI: 10.1029/2003WR002262.
- Cardiff, M., W. Barrash, P.K. Kitanidis, B. Malama, A. Revil, S. Straface, and E. Rizzo. 2009. A potential-based inversion of unconfined steady-state hydraulic tomography. *Ground Water* 47, no. 2: 259–270.
- Castagna, M., and A. Bellin. 2009. A Bayesian approach for inversion of hydraulic tomographic data. *Water Resources Research* 45: W04410. DOI: 10.1029/2008WR007078.
- Craig, A.J. 2005. Measurement of hydraulic parameters at multiple scales in two synthetic heterogeneous aquifers constructed in the laboratory. M.S. thesis, Department of Civil and Environmental Engineering, University of Iowa, Iowa City.
- Fernández-García, D., H. Rajaram, and T.H. Illangasekare. 2005. Assessment of the predictive capabilities of stochastic theories in a three-dimensional laboratory test aquifer: Effective hydraulic conductivity and temporal moments of breakthrough curves. *Water Resources Research* 41: W04002. DOI: 10.1029/2004WR003523.
- Fienen, M.N., T. Clemo, and P.K. Kitanidis. 2008. An interactive Bayesian geostatistical inverse protocol for hydraulic tomography. *Water Resources Research* 44: W00B01. DOI: 10.1029/2007WR006730.
- Gelhar, L.W. 1993. *Stochastic Subsurface Hydrology*. Englewood Cliffs, New Jersey: Prentice-Hall.
- Gelhar, L.W., and C.L. Axness. 1983. Three-dimensional analysis of macrodispersion in a stratified aquifer. *Water Resources Research* 19, no. 1: 161–180. DOI: 10.1029/WR019i001p00161.
- Gottlieb, J., and P. Dietrich. 1995. Identification of the permeability distribution in soil by hydraulic tomography. *Inverse Problems* 11, no. 2: 353–360. DOI: 10.1088/0266-5611/11/2/005.

- Illman, W.A., J. Zhu, A.J. Craig, and D. Yin. 2010a. Comparison of aquifer characterization approaches through steady state groundwater model validation: A controlled laboratory sandbox study. *Water Resources Research* 46: W04502. DOI: 10.1029/2009WR007745.
- Illman, W.A., S.J. Berg, X. Liu, A.J. Craig, and A. Massi. 2010b. Hydraulic/partitioning tracer tomography for trichloroethene source zone characterization: Small-scale sandbox experiments. *Environmental Science and Technology* 44, no. 22: 8609–8614. DOI: 10.1021/es101654j.
- Illman, W.A., X. Liu, S. Takeuchi, T.J. Yeh, K. Ando, and H. Saegusa. 2009. Hydraulic tomography in fractured granite: Mizunami Underground Research site, Japan. *Water Resources Research* 45: W01406. DOI: 10.1029/2007WR006715.
- Illman, W.A., A.J. Craig, and X. Liu. 2008. Practical issues in imaging hydraulic conductivity through hydraulic tomography. *Ground Water* 46, no. 1: 120–132.
- Illman, W.A., X. Liu, and A. Craig. 2007. Steady-state hydraulic tomography in a laboratory aquifer with deterministic heterogeneity: Multi-method and multiscale validation of hydraulic conductivity tomograms. *Journal of Hydrology* 341, nos. 3–4: 222–234.
- Konikow, L.F. 2011. The secret to successful solute-transport modeling. *Ground Water* 49, no. 2: 144–159. DOI: 10.1111/j.00764.x.
- LeBlanc, D.R., S.P. Garabedian, K.M. Hess, L.W. Gelhar, R.D. Quadri, K.G. Stollenwerk, and W.W. Wood. 1991. Large-scale natural gradient tracer test in sand and gravel, Cape Cod, Massachusetts: 1. Experimental design and observed tracer movement. *Water Resources Research* 27, no. 5: 895–910. DOI: 10.1029/91WR00241.
- Li, W., A. Englert, O.A. Cirpka, J. Vanderborght, and H. Vereecken. 2007. Two-dimensional characterization of hydraulic heterogeneity by multiple pumping tests. *Water Resources Research* 43: W04433. DOI: 10.1029/2006WR005333.
- Li, W., W. Nowak, and O.A. Cirpka. 2005. Geostatistical inverse modeling of transient pumping tests using temporal moments of drawdown. *Water Resources Research* 41: W08403. DOI: 10.1029/2004WR003874.
- Li, B., and T.-C.J. Yeh. 1999. Cokriging estimation of the conductivity field under variably saturated flow conditions. *Water Resources Research* 35, no. 12: 3663–3674.
- Liu, X., and P.K. Kitanidis. 2011. Large-scale inverse modeling with an application in hydraulic tomography. *Water Resources Research* 47: W02501. DOI: 10.1029/2010WR009144.
- Liu, X., W.A. Illman, A.J. Craig, J. Zhu, and T.-C.J. Yeh. 2007. Laboratory sandbox validation of transient hydraulic tomography. *Water Resources Research* 43: W05404. DOI: 10.1029/2006WR005144.
- Liu, S., T.-C.J. Yeh, and R. Gardiner. 2002. Effectiveness of hydraulic tomography: sandbox experiments. *Water Resources Research* 38. DOI: 10.1029/2001WR000338.
- Mackay, D.M., D.L. Freyberg, P.V. Roberts, and J.A. Cherry. 1986. A natural gradient experiment on solute transport in a sand aquifer 1. Approach and overview of plume movement. *Water Resources Research* 22, no. 13: 2017–2029.
- Mas-Pla, J., T.-C.J. Yeh, J.F. McCarthy, and T.M. Williams. 1992. Numerical simulation of a two-well tracer experiment. *Ground Water* 30, no. 6: 958–964.
- McCarthy, J., B. Gu, L. Liang, J. Mas-Pla, T. Williams, and T.-C. Yeh. 1996. Field tracer tests on the mobility of natural organic matter in a sandy aquifer. *Water Resources Research* 32, no. 5: 1223–1238.
- Ni, Chuen-Fa, T.-C.J. Yeh, and J.-S. Chen. 2009. Cost-effective hydraulic tomography surveys for predicting flow and transport in heterogeneous aquifers. *Environmental Science and Technology* 43, no. 10: 3720–3727.
- Rehfeldt, K.R., J.M. Boggs, and L.W. Gelhar. 1992. Field study of dispersion in heterogeneous aquifer: 3. Geostatistical analysis of hydraulic conductivity. *Water Resources Research* 28, no. 12: 3309–3324. DOI: 10.1029/92WR01758.
- Straface, S., T.-C.J. Yeh, J. Zhu, S. Troisi, and C.H. Lee. 2007. Sequential aquifer tests at a well field, Montalto Uffugo Scalo, Italy. *Water Resources Research* 43: W07432. DOI: 10.1029/2006WR005287.
- Sudicky, E. 1986. A natural gradient experiment on solute transport in a sand aquifer: Spatial variability of hydraulic conductivity and its role in the dispersion process. *Water Resources Research* 22, no. 13: 2069–2082.
- Sudicky, E.A., W.A. Illman, I.K. Goltz, J.J. Adams, and R.G. McLaren. 2010. Heterogeneity in hydraulic conductivity and its role on the macroscale transport of a solute plume: From measurements to a practical application of stochastic flow and transport theory. *Water Resources Research* 46: W01508. DOI: 10.1029/2008WR007558.
- Wolf, S.H. 1988. Spatial variability of hydraulic conductivity in a sand and gravel aquifer. Eng. thesis, Department of Civil Engineering, Massachusetts Institute of Technology, Cambridge.
- Xiang, J., T.-C.J. Yeh, C.-H. Lee, K.-C. Hsu, and J.-C. Wen. 2009. A simultaneous successive linear estimator and a guide for hydraulic tomography analysis. *Water Resources Research* 45: W02432. DOI: 10.1029/2008WR007180.
- Yeh, T.-C., and J. Zhang. 1996. A geostatistical inverse method for variably saturated flow in the vadose zone. *Water Resources Research* 32, no. 9: 2757–2766.
- Yeh, T.-C.J. 1992. Stochastic modeling of groundwater flow and solute transport in aquifers. *Journal of Hydrologic Processes* 6, no. 4: 369–395.
- Yeh, T.-C.J., and J. Zhu. 2007. Hydraulic/partitioning tracer tomography for characterization of dense nonaqueous phase liquid source zones. *Water Resources Research* 43: W06435. DOI: 10.1029/2006WR004877.
- Yeh, T.-C.J., and C.-H. Lee. 2007. Time to change the way we collect and analyze data for aquifer characterization. *Ground Water* 45, no. 2: 116–118.
- Yeh, T.-C.J., and S. Liu. 2000. Hydraulic tomography: Development of a new aquifer test method. *Water Resources Research* 36, no. 8: 2095–2105.
- Yeh, T.-C.J., M. Jin, and S. Hanna. 1996. An iterative stochastic inverse approach: Conditional effective transmissivity and head fields. *Water Resources Research* 32, no. 1: 85–92.
- Yeh, T.-C.J., A.L. Gutjahr, and M.H. Jin. 1995a. An iterative cokriging-like technique for ground water flow modeling. *Ground Water* 33, no. 1: 33–41.
- Yeh, T.-C.J., J. Mas-Pla, T.M. Williams, and J.F. McCarthy. 1995b. Observation and three-dimensional simulation of chloride plumes in a sandy aquifer under forced-gradient conditions. *Water Resources Research* 31, no. 9: 2141–2157.
- Yeh, T.-C.J., R. Srivastava, A. Guzman, and T. Harter. 1993. A numerical model for water flow and chemical transport in variably saturated porous media. *Ground Water* 31, no. 4: 634–644.
- Yin, D., and W.A. Illman. 2009. Hydraulic tomography using temporal moments of drawdown recovery data: A laboratory sandbox study. *Water Resources Research* 45: W01502. DOI: 10.1029/2007WR006623.
- Zhu, J., and T.-C.J. Yeh. 2006. Analysis of hydraulic tomography using temporal moments of drawdown recovery data. *Water Resources Research* 42: W02403. DOI: 10.1029/2005WR004309.
- Zhu, J., and T.-C.J. Yeh. 2005. Characterization of aquifer heterogeneity using transient hydraulic tomography. *Water Resources Research* 41: W07028. DOI: 10.1029/2004WR003790.